# Simulation of Shock/Boundary-Layer Interactions with Bleed Using Immersed-Boundary Methods

Santanu Ghosh,* Jung-Il Choi,† and Jack R. Edwards‡
*North Carolina State University, Raleigh, North Carolina 27695-7910*

DOI: 10.2514/1.45297

This work uses an immersed-boundary method to simulate the effects of arrays of discrete bleed holes in controlling shock-wave/turbulent-boundary-layer interactions. Both Reynolds-averaged Navier–Stokes and hybrid large-eddy/Reynolds-averaged Navier–Stokes turbulence closures are used with the immersed-boundary technique. The approach is validated by conducting simulations of Mach 2.5 flow over a perforated plate containing 18 individual bleed holes. Computed values of discharge coefficient as a function of bleed plenum pressure are compared to experimental data. Simulations of an impinging-oblique-shock/boundary-layer interaction at Mach 2.45 with and without bleed control are also performed. For the studies with bleed, two different bleed rates are employed. The 68 hole bleed plate is rendered as an immersed object in the computational domain. Wall pressure predictions show that, in general, the large-eddy/Reynolds-averaged Navier–Stokes technique underestimates the upstream extent of axial separation that occurs in the absence of bleed. Good agreement with pitot pressure surveys throughout the interaction region is obtained, however. Flow control at the maximum-bleed rate completely removes the separation region and induces local disturbances in the wall pressure distributions that are associated with the expansion of the boundary-layer fluid into the bleed port and its subsequent recompression. Computed pitot pressure distributions are in good agreement with experiment for the cases with bleed. Swirl-strength probability density distributions are used to estimate the evolution of turbulent length scales throughout the interaction. These, along with Reynolds-stress predictions, indicate that an effect of strong bleed rates is to accelerate the recovery of the boundary layer toward a new equilibrium state downstream of the interaction region.

## Nomenclature

| | | |
|---|---|---|
| $a_1$ | = | model constant for Menter baseline model |
| $C_f$ | = | skin-friction coefficient |
| $C_M$ | = | model constant for mixed-scale model |
| $C_\mu$ | = | model constant for Menter baseline model |
| $D$ | = | diameter of bleed hole |
| $d$ | = | distance from nearest-wall/immersed-surface point |
| $d^{+,-}$ | = | normalized distance |
| $F_2$ | = | model constant for Menter baseline model |
| $f, g$ | = | scaling functions |
| $G$ | = | Heaviside step function based on signed distance function |
| $k$ | = | turbulent kinetic energy/power law |
| $L$ | = | length of bleed hole |
| $M$ | = | Mach number |
| $\mathbf{n}$ | = | coordinate normal to immersed surface |
| $P$ | = | static pressure |
| $P_t$ | = | pitot pressure |
| $Q$ | = | sonic flow coefficient or discharge coefficient |
| $q^2$ | = | estimate of subgrid kinetic energy |
| $R$ | = | universal gas constant |
| $Re$ | = | Reynolds number |
| $R_i^{n+1,l}$ | = | residual vector at cell $i$ for time step $n+1$ and subiteration $l$ |
| $r$ | = | recovery factor |
| $S$ | = | characteristic filtered rate of strain |
| $T$ | = | temperature |
| $u$ | = | velocity vector, $x$ component of velocity |
| $u_\tau$ | = | friction velocity |
| $V$ | = | primitive variable vector |
| $v$ | = | component of velocity in $y$ direction |
| $w$ | = | component of velocity in $z$ direction |
| $X$ | = | streamwise distance from leading edge of bleed-plate insert |
| $x$ | = | streamwise distance from leading edge of computational domain |
| $Y$ | = | vertical distance from lower wall |
| $Z$ | = | spanwise distance measured from centerline of domain/wind tunnel |
| $\gamma$ | = | ratio of specific heats |
| $\Delta$ | = | grid size and filter width for large-eddy simulation model |
| $\delta$ | = | boundary-layer thickness |
| $\delta^*$ | = | displacement thickness |
| $\eta$ | = | ratio of wall distance to modeled Taylor microscale |
| $\theta$ | = | momentum thickness |
| $\kappa$ | = | model parameter |
| $\lambda_0$ | = | swirl strength |
| $\mu_t$ | = | dynamic eddy viscosity |
| $\nu_t$ | = | kinematic eddy viscosity |
| $\rho$ | = | density |
| $\tilde{\rho}$ | = | normalized density |
| $\Phi$ | = | signed distance function |
| $\chi$ | = | modeled form of Taylor microscale |
| $\Omega$ | = | mean vorticity |
| $\omega$ | = | turbulence frequency |

*Subscripts*

| | | |
|---|---|---|
| $B$ | = | at band cell |
| $I$ | = | at interpolation point |
| $i$ | = | $i$th component of vector |
| $j$ | = | $j$th component of vector |
| $M$ | = | mixed-scale model |
| $N$ | = | normal component |

*Ph.D. Student, Department of Mechanical and Aerospace Engineering. Student Member AIAA.
†Research Assistant Professor, Department of Mechanical and Aerospace Engineering. Member AIAA.
‡Professor, Department of Mechanical and Aerospace Engineering. Associate Fellow AIAA.

| | | |
|---|---|---|
| $o$ | = | total |
| ref | = | conditions at upstream reference plane |
| $S$ | = | at surface |
| $T$ | = | tangential component |
| $w$ | = | at wall |
| $\infty$ | = | freestream |

*Superscripts*

| | | |
|---|---|---|
| $l$ | = | subiteration level |
| $n$ | = | time step |
| $+$ | = | between band cell and interpolation point |
| $-$ | = | between immersed surface and band cell |

## I.  Introduction

THE control of shock-induced separation within a supersonic inlet is critical in achieving the desired total pressure recovery and uniformity of the flow entering the compressor. Offdesign responses, such as inlet unstart, are often the result of the growth of large regions of separated flow, generated initially through shock interactions. Control of shock-induced separation within the inlet often involves the use of bleed systems and slots to skim off a portion of the boundary layer [1–5]. The design of bleed systems for high-speed inlets is an area in which experimentation and empirical correlations have played a dominant role [3,4]. Most efforts in the simulation of boundary-layer bleed for separation control have concentrated on single slot or hole effects [5–8], though some studies that consider multiple holes within a periodic array have been reported [9,10]. With the exception of a few three-dimensional studies involving resolution of individual holes using overset-grid [9] or unstructured-mesh [10] techniques, most studies have assumed two-dimensional flow, and all have used Reynolds-averaged Navier–Stokes (RANS) models or simpler strategies. Given the fact that shock/boundary-layer interactions tend to be unsteady on a large scale, and that local pressure differences can lead to periodic blowing/suction even in active control devices [11], it appears that accounting for the time-dependent nature of the control approach and its interaction with the flow may be critical to achieving better predictions. The geometric complexity of bleed systems complicates the application of techniques, such as large-eddy simulation (LES), as resolution of features, such as individual holes, would normally require a large number of clustered mesh cells. The number of mesh points used could become excessively large, and the accuracy of the LES approach could diminish because of the presence of large numbers of irregular mesh cells.

This paper is part of a general thrust toward developing immersed-boundary (IB) methods capable of simulating the effects of various flow-control devices used in high-speed internal flows. The potential advantages of an IB method in this scope include significant economy in the number of mesh points required in the vicinity of the control device (compared to body-fitted meshes), the ease in which different types of control devices can be interchanged and their effects assessed, and the ability to model moving control devices (such as mesoflaps) without mesh adaptation. An IB method that is suitable for these applications has been recently developed for incompressible flows [12] and has been extended to compressible flows in [13]. This approach reconstructs the velocity field near immersed surfaces using a power-law function, which enables the method to approximate the energizing effects of a turbulent boundary layer. This eliminates the need for a highly resolved mesh near the immersed body. The use of the technique to simulate the effects of micro vortex generators in controlling shock/boundary-layer interactions [13] and initiating transition to turbulence in hypersonic boundary layers [14] has been reported. In all cases, the IB method provides predictions similar to those obtained on body-fitted meshes. In this paper, we apply the compressible IB method in conjunction with RANS [15] and LES/RANS [16] turbulence models to several problems involving boundary-layer suction through bleed-hole arrays. Experiments conducted at NASA John H. Glenn Research Center (GRC) at Lewis Field involving boundary-layer flow over perforated plates [17] and shock/boundary-layer interactions with and without active bleed [18] are used to assess the methodology. The outline of this paper is as follows. Section II describes the computational model, including details of the flow solver, the turbulence closures used, and the IB method. Section III describes the problem setup, including details of the experiments simulated, the meshing arrangement, and boundary conditions. Results of the investigation are presented in Sec. IV, and some conclusions are outlined in Sec. V.

## II.  Computational Methodology

The governing compressible Navier–Stokes equations are discretized in a finite volume framework. Inviscid fluxes are discretized using a low-diffusion flux-splitting scheme (LDFSS) [19], while viscous and diffusive fluxes are discretized using second-order central differences. The piecewise parabolic method [20] is used to extend the first-order LDFSS upwind scheme to fourth order in smooth regions of the flow. A dual-time-stepping implicit method is used to advance the equations in time. At each time step, a Crank–Nicholson discretization of the equations is solved to a prescribed tolerance using a subiteration procedure. The matrix system resulting from the linearization of the equation system is approximately solved using a planar relaxation procedure at each subiteration.

The present work adopts two nonstandard techniques: a hybrid LES/RANS modeling strategy designed for high-speed wall-bounded compressible flows and an extension of an existing immersed-boundary method to compressible turbulent flows. Each component is described briefly in the following sections.

### A.  RANS and Hybrid LES/RANS Methodology

In the present study, the RANS closure used is Menter's hybrid $k$-$\omega$/$k$-$\varepsilon$ model [15] in its baseline (BSL) and shear-stress transport (SST) forms. Specifically, the BSL model is used for RANS cases without shock impingement, and the SST model is used for the shock-interaction cases. The SST model generally increases the extent of separation, relative to the BSL model, and for this case, the adoption of the SST modification results in better agreement with experimental data. The Menter BSL model is used as the RANS component of the hybrid LES/RANS model, as previous studies [16,21] have found that this approach provides generally better results than the use of the SST model.

The hybrid LES/RANS model used in the present study [16] involves only modifications to the eddy viscosity description:

$$\mu_t = \rho v_t = \rho\left(\Gamma \frac{a_1 k}{\max(a_1\omega, A_{\mathrm{sst}}\Omega F_2)} + (1-\Gamma)v_{t,M}\right)$$
$$A_{\mathrm{sst}} = 0 \tag{1}$$

As the blending function approaches one, the closure approaches its RANS description, and as it approaches zero, a subgrid eddy viscosity is obtained. This work uses a mixed-scale model [22] for the subgrid eddy viscosity, defined as

$$v_{t,M} = C_M S^{\frac{1}{2}}(q^2)^{\frac{1}{4}}\Delta^{\frac{3}{2}}, \qquad C_M = 0.06$$
$$S = \left[\frac{\partial \tilde{u}_i}{\partial x_j}\frac{\partial \tilde{u}_j}{\partial x_i} + \frac{\partial \tilde{u}_i}{\partial x_j}\frac{\partial \tilde{u}_i}{\partial x_j} - \frac{2}{3}\left(\frac{\partial \tilde{u}_i}{\partial x_i}\right)^2\right]^{\frac{1}{2}} \tag{2}$$

An estimate of the subgrid kinetic energy is obtained by test filtering the resolved-scale velocity data:

$$q^2 = \frac{1}{2}(\tilde{u}_k - \hat{\tilde{u}}_k)^2 \tag{3}$$

The blending function $\Gamma$ is based on the ratio of the wall distance to a modeled form of the Taylor microscale:

$$\Gamma = \frac{1}{2}\left(1 - \tanh\left[5\left(\frac{\kappa}{\sqrt{C_\mu}}\eta^2 - 1\right) + \phi\right]\right), \qquad \eta = \frac{d}{\alpha\chi} \tag{4}$$

where $\phi$ is set to $\tanh^{-1}(0.98)$ in order to fix the balancing position (where $\kappa\eta^2 = \sqrt{C_\mu}$) to $\Gamma = 0.99$. The Taylor microscale is defined as $\chi = \sqrt{\nu/C_\mu\omega}$. The constant $\alpha$ is chosen to enforce the average LES to RANS transition ($\Gamma = 0.99$ position) for equilibrium boundary layers at the point where the wake law starts to deviate from the log law. The procedure for doing this is presented in Edwards et al. [16] and Choi et al. [23]. When applied to the entire development of the boundary layer in the computational domain considered in this study, this procedure leads to a spatially varying form for the model constant $\alpha$ that is fit as $\alpha(x) = 53.90 + 11.04x$, with $x$ being the distance from the leading edge of the computational domain ($-0.3181$ m). To initiate and sustain large turbulent structures, a recycling/rescaling procedure [16,24,25] applied to the fluctuating fields is used.

## B.  Immersed Boundary Method

In the present work, a compressible extension [13] of an IB method developed in Choi et al. [12] is used. The immersed surface is generated as a cloud of points, which can be structured or unstructured. The entire flow domain is then classified into three categories of cells. Cells sufficiently removed from the immersed boundary are termed as field cells, cells very near but not inside the immersed object are band cells, and cells inside the immersed body are interior cells (see Fig. 1). To perform this classification, a distance function to the nearest surface point for all cells (within a bounding box of the IB) is computed using an approximate nearest-neighbor search algorithm. Concepts from computational geometry are then used to impose an unambiguous sign to the distance function (thus deciding inside or outside for closed surfaces). A direct forcing approach is used to enforce the boundary conditions at the interior and band cells. Band-cell properties are defined by interpolation of information from surrounding field cells along lines normal to the surface. This results in the residual form of the equation system shown below, which is then solved implicitly, coupled with exterior cells, by use of subiteration techniques:

$$R_i^{n+1,l} = (1 - G(\Phi^{n+1}))R_{i,\mathrm{NS}}^{n+1,l} + G(\Phi^{n+1})\left[\frac{V_i^{n+1,l} - V_{B,i}^{n+1,l}}{\Delta t}\right] = 0 \tag{5}$$

This equation represents the blending of the Navier–Stokes residual with a source term that relaxes the primitive variable vector $V$ to its band-cell values. The quantity $G$ is a sharp Heaviside function (set to 1 for band and interior cells and zero otherwise), $\Phi$ is the signed distance function, and $l$ is a subiteration index. To extend the method to compressible flows, the following first-order-accurate closures are considered for the fluid properties in the band cells, where the subscript $I$ indicates properties obtained at an interpolation point located along the normal line extending outward from the nearest surface point corresponding to the band cell in question, and the subscript $B$ indicates the band cell [12]:
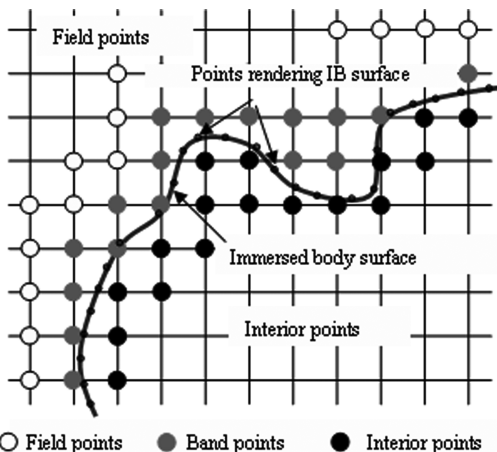


O Field points  ● Band points  ● Interior points
**Fig. 1   Cell classification scheme for immersed-boundary method.**

$$u_{B,i} - u_{S,i} = u_{T,i}(d_I)\left(\frac{d_B}{d_I}\right)^k + u_{N,i}(d_I)g(\rho, d_I, d_B)$$

$$u_{N,i}(d_I) = (u_j(d_I) - u_{S,j})\mathbf{n}_j\mathbf{n}_i$$

$$u_{T,i}(d_I) = (u_i(d_I) - u_{S,i}) - u_{N,i}(d_I) \tag{6}$$

In these expressions, $\mathbf{n}_i$ is the normal vector at the closest point on the body surface, $d$ is a distance from the nearest surface point, and $k$ is a power law. The choice of $k$ allows the model to replicate a turbulent velocity profile ($k = 1/7$ or $1/9$) or a laminar profile ($k = 1$). To obtain the temperature distribution near the surface, Walz's relation for the temperature distribution within an adiabatic, compressible boundary layer is used [26]:

$$\frac{T_B}{T(d_I)} = 1 + \frac{r(\gamma - 1)}{2\gamma RT(d_I)}[u_{T,i}(d_I)]^2\left(1 - \left(\frac{d_B}{d_I}\right)^{2k}\right) \tag{7}$$

In this equation, $r$ is the recovery factor and $[u_{T,i}(d_I)]^2$ is the kinetic energy associated with the tangential velocity component at the interpolation point. The density in the band cells is obtained by solving the continuity equation, subject to zero-flux conditions imposed wherever the distance function changes sign at a cell interface and to the velocity field defined above. The turbulence variables in the band cells are defined as

$$k_B = \frac{u_\tau^2}{\sqrt{C_\mu}}, \qquad \omega_B = \frac{u_\tau}{\sqrt{C_\mu}\kappa d_B} \quad : d^+ > 10.934$$

$$k_B = k(d_I)\left(\frac{d_B}{d_I}\right)^2, \qquad \omega_B = \frac{60\nu_w}{0.075d_B^2} \quad : d^+ < 10.934 \quad \text{or} \quad k = 1$$

$$d^+ = \frac{u_\tau d_b}{\nu_w}, \qquad u_\tau = \frac{|u_{T,i}(d_I)|}{(\ell n(d^+)/\kappa + 5.1)} \tag{8}$$

In Eq. (8), $d^+$ and $u_\tau$ are solved iteratively. The function that scales the normal velocity component in Eq. (6) is determined by enforcing a discrete form of the continuity equation at each band cell [13]. The result for an adiabatic wall is given as

$$g(\rho, d_I, d_B) = \frac{1}{\tilde{\rho}}\frac{\dfrac{d_B}{d_I}d^-\tilde{\rho}^-}{\left(\dfrac{d_B}{d_I}d^-\tilde{\rho}^- + \left(1 - \dfrac{d_B}{d_I}\right)\tilde{\rho}^+\right)}$$

$$d^- = \left(\frac{d_B}{2d_I}\right)^k, \qquad d^- = \left(\frac{1}{2}\left(1 + \frac{d_B}{d_I}\right)\right)^k$$

$$\frac{1}{\tilde{\rho}} = 1 + \frac{r(\gamma - 1)}{2\gamma RT(d_I)}[u_{T,i}(d_I)]^2\left(1 - \left(\frac{d_B}{d_I}\right)^{2k}\right)$$

$$\frac{1}{\tilde{\rho}^-} = 1 + \frac{r(\gamma - 1)}{2\gamma RT(d_I)}[u_{T,i}(d_I)]^2(1 - (d^-)^2)$$

$$\frac{1}{\tilde{\rho}^+} = 1 + \frac{r(\gamma - 1)}{2\gamma RT(d_I)}[u_{T,i}(d_I)]^2(1 - (d^+)^2) \tag{9}$$

## III.  Problem Setup

### A.  Experiment Details

Experiments involving the effects of boundary-layer bleed on shock-interaction control were performed at NASA GRC by Willis et al. [18]. The experiments were performed at a nominal Mach number of 2.46, a stagnation temperature of 292 K, and a stagnation pressure of 172.4 kPa. Other parameters are summarized in Table 1. In the configuration, an 8 deg wedge was placed so that the generated oblique shock impinged in the middle of a 9.52 cm bleed region embedded within the wind-tunnel lower surface. This region consisted of a regular array of 100 circular holes with diameter $D = 0.635$ cm and length $L = 0.635$ cm and oriented 90 deg with respect to the plate surface The bleed flow exited into a plenum chamber, and the rate of mass flow out of the system was controlled by a regulator and driven by a vacuum generated by a 450 psi air ejector system. Both the plenum pressure and overall bleed mass flow were recorded in the experiments. Data collected in these experiments included

**Table 1   Freestream and boundary-layer conditions for Willis et al. [18] shock/boundary-layer experiments**

| | |
|---|---|
| $M_\infty$ | 2.46 |
| $p_o$, kPa | 172.4 |
| $T_o$, K | 292.0 |
| $Re/m$ | $1.81 \times 10^7$ |
| $\delta_{\text{ref}}$, cm | 2.63 |
| $\delta^*_{\text{ref}}$, cm | 0.727 |
| $\theta_{\text{ref}}$, cm | 0.196 |
| $C_f$ | $1.43 \times 10^{-3}$ |

pitot pressure surveys at different streamwise locations, wall static pressure distributions, and pitot pressure surveys taken in the bleed-region exit plane, all as a function of the bleed mass flow rate. In the experiments, the bleed mass flow rate is expressed as a discharge coefficient $Q$, representing the ratio of the actual bleed rate to the ideal value obtained under choked-flow conditions. Data was obtained for three values of $Q$, 0.00, 0.0342, and 0.0685, as well as for a baseline case in which the bleed plate was replaced by a solid surface. This case differs from the $Q = 0.00$ case, as the latter allows bleed into, and injection out of, the plenum. Except for the zero-bleed case ($Q = 0.0$), all other cases are considered in this study.

In addition to the Willis et al. [18] shock/boundary-layer experiment, calculations were also performed for an experiment involving Mach 2.45 boundary-layer flow over a bleed plate [17]. This experiment focused on quantifying the discharge coefficient as a function of hole size, hole angle, plenum pressure, and freestream conditions. The hole shape is the same as in [18], but the spacing of the holes within the array is different. Table 2 summarizes the flow conditions for this experiment.

### B.   Computational Domain

The computational domain for the Willis et al. [17] flat-plate boundary-layer simulations extends from $X = -5.08$ to 17.78 cm in the streamwise direction, from $Y = 0$ to 7.62 cm in the wall-normal direction, and from $Z = -1.905$ to 1.905 cm in the spanwise direction. The bleed plenum for this case ranges from $X = -1.905$ to 9.525 cm and from $Y = -7.62$ to $-0.635$ cm, and the bleed-hole region extends from $X = 0$ to 7.62 cm and from $Y = -0.635$ to 0 cm. To provide better resolution near the bleed ports, the meshes covering the bleed region are refined by a factor of 2 in the $Z$ direction. A patched-mesh boundary condition [27] is used to facilitate the coarse-to-fine and fine-to-coarse information transfers in this region. The $X$-$Z$ resolution is sufficient to cover each circular bleed hole with a $10 \times 10$ square mesh. The total number of cells is 3.24 million, with 2.268 million located above the flat plate, 0.432 million within the bleed-hole region, and 0.540 million in the plenum. The bleed plate itself is generated as a combination of surfaces: two flat plates with cutout holes for the top and bottom portions and 18 hollow cylinders ($L = 0.635$ cm and $D = 0.635$ cm) for the hole walls. A relatively fine IB surface mesh, containing 1.32 million points, was used to ensure an accurate distance-function evaluation, as the method employed in this work does not search within individual panels for the true nearest distance. Figure 2 shows the immersed-surface rendition of one circular cylinder (hole wall) and the surrounding mesh.

**Table 2   Freestream and boundary-layer conditions for Willis et al. [17] flat-plate boundary-layer experiments**

| | |
|---|---|
| $M_\infty$ | 2.46 |
| $p_o$, kPa | 172.4 |
| $T_o$, K | 293.0 |
| $Re/m$ | $1.75 \times 10^7$ |
| $\delta_{\text{ref}}$, cm | 2.63 |
| $\delta^*_{\text{ref}}$, cm | 0.727 |
| $\theta_{\text{ref}}$, cm | 0.198 |
| $C_f$ | $1.29 \times 10^{-3}$ |
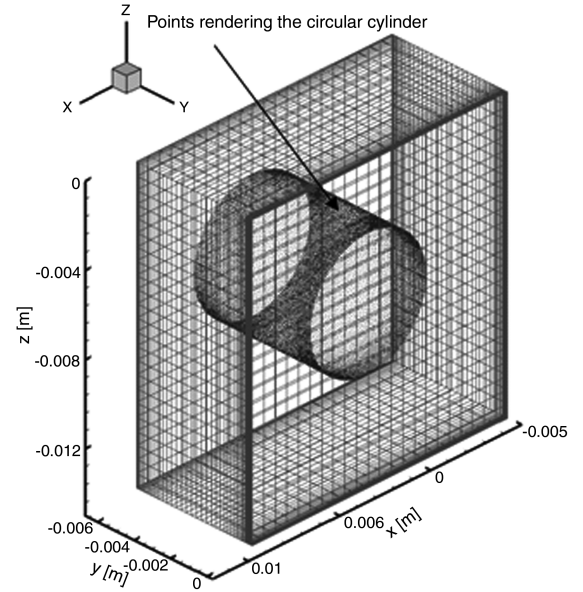


**Fig. 2   Mesh around the IB rendition of a circular bleed hole.**

The computational domain for the Willis et al. [18] shock/boundary-layer interaction simulations extends from $X = -31.81$ to 25.0 cm in the streamwise direction, from $Y = 0.0$ to 21.5 cm in the wall-normal direction at the inflow plane, and from $Z = -5.08$ to 5.08 cm in the spanwise direction. The upper boundary is aligned with the position of the 8 deg shock generator. The nominal mesh spacing in the $X$ and $Z$ directions is 0.13 cm, decreasing to half of this value in the portions of the mesh covering the bleed region. The meshes covering the bleed-region range from $X = -2.23$ to 13.01 cm and from $Y = -2.5$ to 0.0 cm. The plenum chamber extends from $X = -14.5$ to 26 cm at the upper end (end of bleed region: $Y = -2.5$ cm) and from $X = -3.82$ to 15.82 cm at the exit ($Y = -24.64$ cm) The cross section of the plenum is rectangular until about $Y = -9.88$ cm and then tapered to the dimensions at the exit using cubic fits. The bleed ports for this case are the same size as in the flat-plate study and the $X$-$Z$ resolution is sufficient to cover each port with $10 \times 10$ square cells. The total number of mesh cells is 21.504 million, with 12.544 million located above the flat plate, 1.792 million located in the portion of the domain covering the bleed holes, another 1.792 million in the region between the bleed holes and the plenum, and 5.376 million located in the plenum. The bleed-plate surface mesh contains 4.367 million points and is composed of two flat sections with cutout holes and 68 individual hollow cylinders.

### C.   Boundary Conditions

No-slip, adiabatic wall boundary conditions are imposed on all solid surfaces (excepting shock generator and plenum walls where a slip-wall condition is imposed) for both cases. A linear power law is used to define the near-surface velocity interpolation for the flat-plate portions of the immersed bleed-plate object, as the mesh spacing near the wall is sufficient to resolve the viscous sublayer. The power law for the portions representing the hole walls was varied as part of the flat-plate boundary-layer study, but, in general, a fractional power law (1/7 or 1/9) is employed, as the mesh resolution near the hole surfaces does not extend into the viscous sublayer. A subsonic outflow condition, which imposes the experimental mass flow rate (using a relaxation technique), is used at the plenum exit. Pressure and temperature are extrapolated and density is calculated based on equation of state. The normal velocity is then fixed based on the value of mass flux imposed and the density. The tangential velocity components are also zeroed out. Periodic boundary conditions are imposed in the spanwise directions. It should be noted that the experiments of Willis et al. [17] used aerodynamic fences to isolate the interaction region from the corner flows developing in the wind tunnel.

The spanwise extent of the computational domain does not extend to the positions of the fences ($\pm 7.94$ cm), and, as such, the calculations represent an idealized shock/boundary-layer interaction free from effects of mean three-dimensionality. For the flat-plate boundary-layer simulations, flow properties are extrapolated from the interior on the upper boundary and the downstream boundary. For the shock/boundary-layer interactions, slip-wall conditions are applied along the upper boundary, and properties are extrapolated from the interior at the downstream boundary.

### D.  Calculation Details

In all cases, a flat-plate simulation at the test-section conditions was performed to determine the place at which the predicted boundary-layer properties most closely matched the experimental data. Flow properties at the inflow plane of the computational domain were then extracted from the flat-plate solution at a location consistent with the position of the inflow plane relative to the measurement location. Convergence of the RANS calculations was ascertained using three measures: relative decrease in residual norm, constancy of surface quantities, and constancy of the global mass flow rate and bleed mass flow rates. The bleed mass flow rates were evaluated at the bleed-hole entrance and exit planes as well as the plenum exit plane. The LES/RANS calculations were initiated by superimposing scaled boundary-layer fluctuations from an earlier calculation onto part of a converged RANS solution. After several flow-through times to eliminate initial transients, time-averaged statistics for the LES/RANS calculations were collected over a minimum of seven flow-through times, based on the domain length and freestream velocity.

## IV.  Results

### A.  Flat-Plate Boundary-Layer Simulations with Bleed

Simulations of Mach 2.5 flow over a perforated plate were performed to ascertain the ability of the methodology to predict the discharge coefficient as a function of plenum pressure. The Menter BSL RANS model was used for these calculations. Mach number contours in Figs. 3 and 4 show the characteristic pattern of flow entrainment into the bleed holes. The immersed-boundary object that represents the bleed plate is shown in Fig. 3. A large pocket of separated flow is formed at the upstream edge of each hole. The near-wall fluid accelerates to supersonic velocities within the bleed port and is forced to change direction, moving down into the plenum. The separation region forms an effective converging/diverging nozzle that first slows the supersonic flow down, then expands it to higher supersonic velocities before entering the plenum. Figure 5 plots the discharge coefficient [actual mass flow rate divided by ideal (isentropic) mass flow rate at sonic conditions] versus the ratio of the plenum pressure to the upstream stagnation pressure. The predictions are seen to be in reasonable agreement with the experimental data. The predicted mass flow rate is a strong function of the power used to define the band-cell velocity field near the hole surfaces. Using a value of $k = 1$ (consistent with a linear near-wall velocity field and laminar flow) leads to too much flow separation within the bleed holes and to a reduction in the discharge coefficient. Values more consistent with a turbulent profile ($k = 1/7$ or $1/9$) promote more flow attachment and provide discharge coefficients more in accord with the experimental data. The predicted discharge coefficients at lower plenum pressures are somewhat smaller than indicated in the experiment and in an earlier calculation that used body-fitted meshes to resolve a small segment of the bleed-hole array [10]. The effect of reducing the $X$-$Z$ mesh resolution over each hole from $10 \times 10$ cells per hole to $5 \times 5$ cells per hole is also shown for the lowest plenum pressure. A reduction in predicted mass flow rate of about 17%, relative to the baseline $10 \times 10$ resolution, is observed.

### B.  Oblique-Shock/Turbulent-Boundary-Layer Interaction Without Bleed

A snapshot of temperature contours along the $X$-$Y$ center plane is shown in Fig. 6 for the baseline shock/boundary-layer interaction
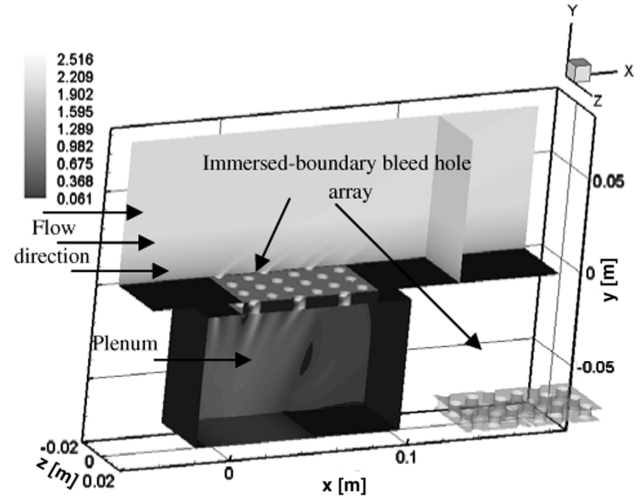


**Fig. 3  Three-dimensional view of flow over a perforated plate with active suction (Mach number contours shown).**
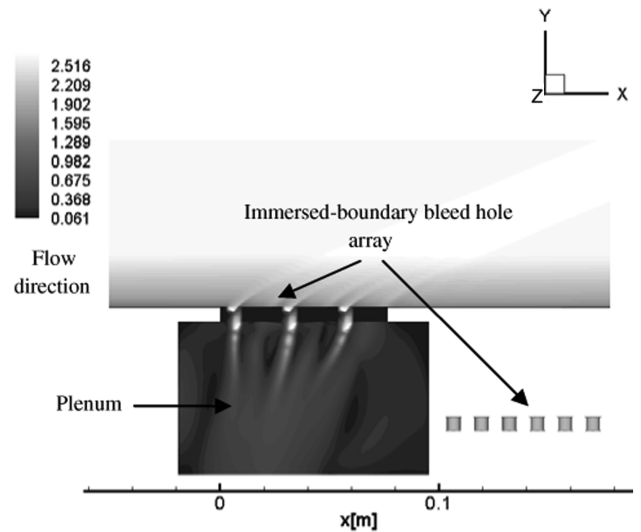


**Fig. 4  $X$-$Y$ view of flow over a perforated plate with active suction (Mach number contours shown).**
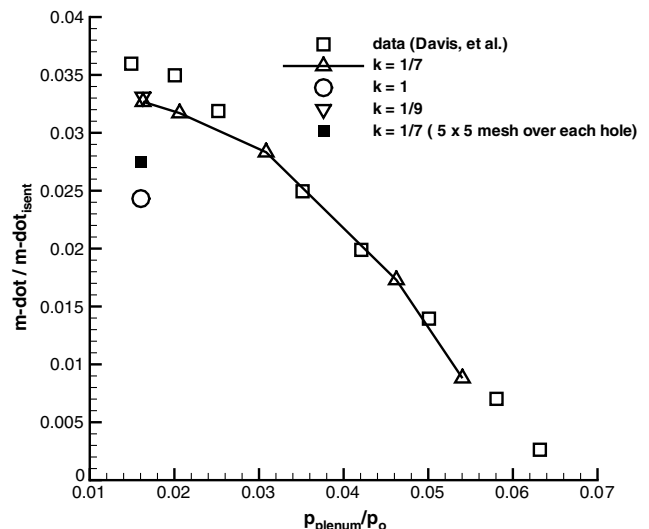


**Fig. 5  Flow coefficient versus plenum pressure.**
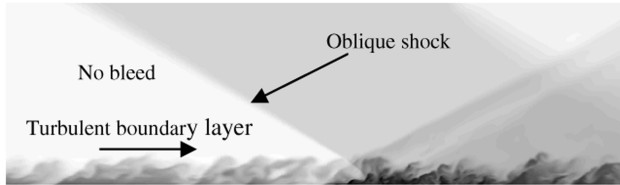
**Fig. 6  Snapshot of center-plane temperature contours for oblique-shock interaction without bleed.**
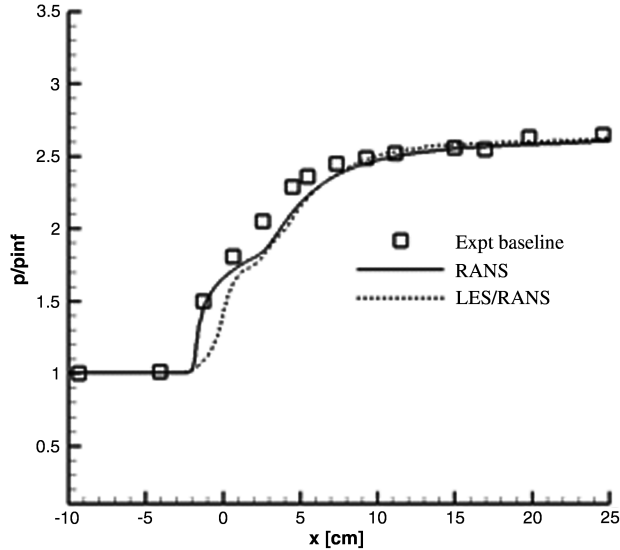


**Fig. 7   Wall pressure distributions: shock/boundary-layer interaction without bleed.**

without bleed. The results indicate a general thinning of the boundary layer downstream of the shock reflection as well as local hot spots (darker contours) caused by turbulent separation and reattachment, as well as by shock interaction. The shock wave is strong enough to induce mild separation of the turbulent boundary layer, as indicated in Fig. 7: a plot of centerline wall pressure. The better agreement with experimental data is provided by the Menter SST RANS model, which correctly predicts the degree of upstream influence shown in the experiment. The LES/RANS model and Menter BSL RANS model (not shown) tend to underpredict the size of the separation region. These results may be viewed with some caution, as computations of an interaction of similar strength in a wind tunnel [13] showed that the interaction of the oblique shock with the sidewall induced a crossflow that caused the separation region on the wind-tunnel floor to bulge toward the centerline. The aerodynamic fences employed in the NASA GRC experiments should mitigate this effect to some degree, but they also induce their own wave interactions. The level of mean three-dimensionality present in the NASA GRC experiments should be quantified in future work.

Centerline pitot pressure distributions throughout the interaction region are shown in Fig. 8 for the LES/RANS and Menter SST model. The first trace of the incident oblique shock is captured at station 4, with the sharp pressure change at ~4 cm from the wall. Stations 5–8 ($x = 3.8, 29.2, 54.5, 80.0$ mm) form the core of the interaction of the oblique shock with the boundary layer. This is expected as these stations are within the bleed plate and the inviscid oblique shock impinges ideally at the center of the bleed region. The experimental data shows the onset of separation in profile 5. Good agreement is generally observed, with some discrepancies in the wakelike profile noted in the LES/RANS predictions at the $X = 3.8$ and 29.2 mm stations. These are related to the underprediction of axial separation noted earlier. In the recovery region, the LES/RANS and RANS predictions generally bracket the experimental data, with the former slightly overpredicting the rate of recovery of the boundary layer.
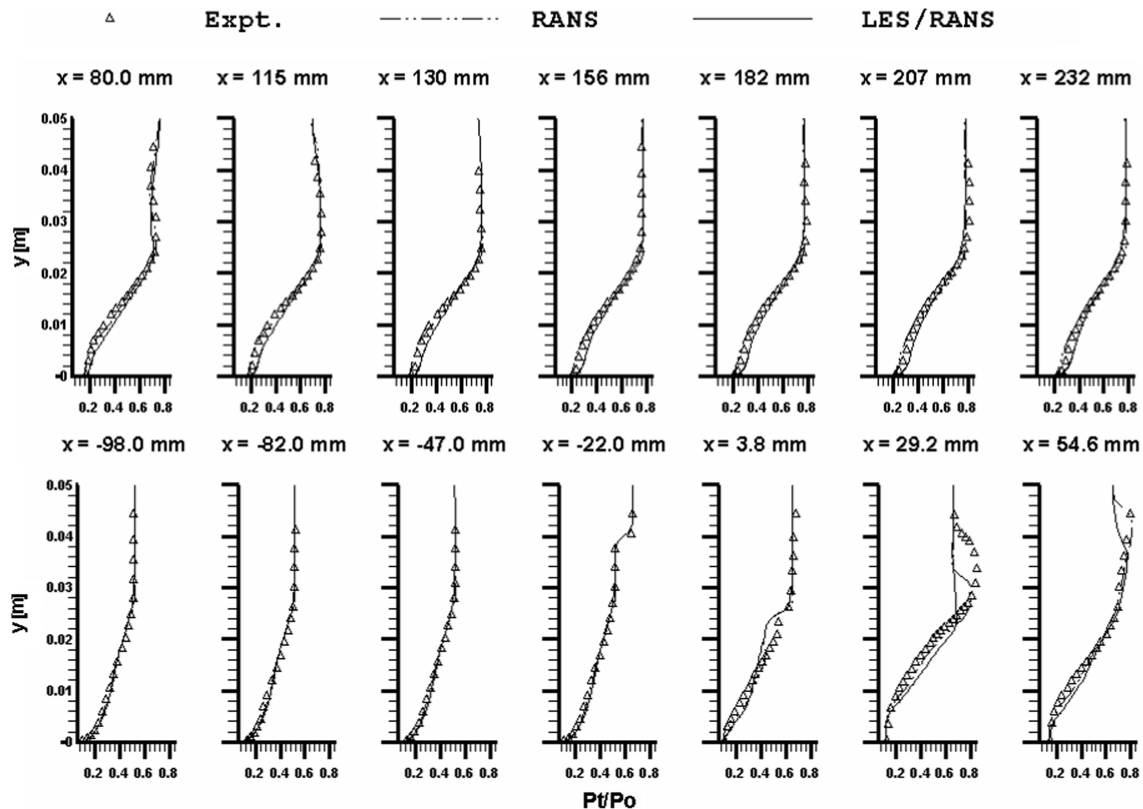


**Fig. 8   Pitot pressure distributions: shock/boundary-layer interaction without bleed.**

## C. Oblique-Shock/Turbulent-Boundary-Layer Interaction with Bleed

The cases detailed in this section involve suction through a 68 hole perforated plate, as shown in Fig. 9 as the zero isosurface of the signed distance function. Two different bleed rates, referred to henceforth as full bleed (maximum bleed) and half-bleed, which is basically half of the maximum bleed, were simulated. Both RANS/LES and RANS simulations were performed for the full-bleed case, while only the LES/RANS model was used for the half-bleed simulation. The experimental and computed (averaged from LES/RANS simulations) values of the flow coefficient are listed in Table 3. Both simulations were initialized with plenum pressures, which correspond to those in the experiment for the respective bleed rates (5534 Pa for full bleed and 17,413 Pa for half-bleed). In the half-bleed case, the bleed mass flow rates are much more unsteady due to periodic blowing and suction through the holes located upstream of the shock-impingement position.

Temperature contours shown in Fig. 9 reveal that the bleed array produces localized wave patterns associated with the formation of expansion waves as the near-wall fluid moves into each bleed port and with the formation of a recompression shock located at the downstream edge of the bleed port. This response occurs for all the bleed ports in the full-bleed case but only in the most downstream (last two) ports for the half-bleed case. A general thinning of the boundary layer within and downstream of the bleed region is evident, as is a recompression shock located just downstream of the end of the bleed region. Overall, the effects are more pronounced for the full-bleed case. Higher temperatures are noted near the vicinity of the shock-impingement position for the half-bleed case. These are associated with a recirculation region formed due to the

**Table 3  Flow coefficients for experiment and computation at different bleed rates.**

| Bleed rate | Experiment | Computational fluid dynamics |
|---|---|---|
| Full bleed | 0.0685 | 0.062 |
| Half-bleed | 0.0342 | 0.034 |

shock impingement and enlarged somewhat by air blowing out from the plenum. The freejet expansion of the bleed-hole fluid as it enters the plenum is less pronounced for in the half-bleed case due to the higher plenum pressure.

Centerline surface pressure distributions in Fig. 10 provide more evidence of the localized expansion/compression events induced by the suction effect. The pressure levels at the surface plane over each bleed port are included in the computational distributions to provide an indication of the local flow patterns. For the full-bleed simulation, the LES/RANS and RANS predictions are very similar, and when averaged to the experimental data locations, are in reasonable agreement with the measurements. Surface pressure predictions for the half-bleed case also compare reasonably well to the data. It is interesting to note that the localized compression and expansion effects are relatively absent in the upper part of the interaction region
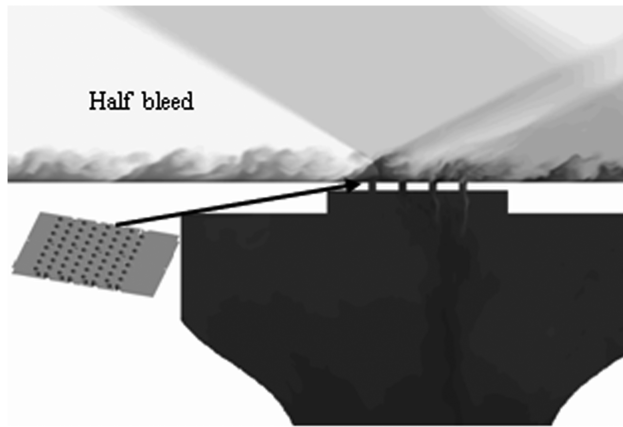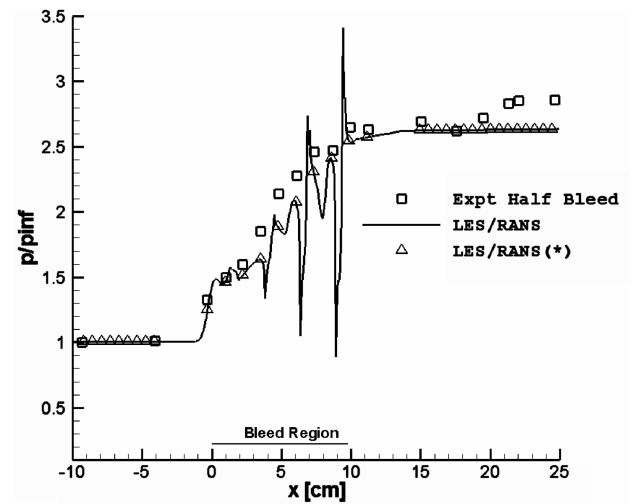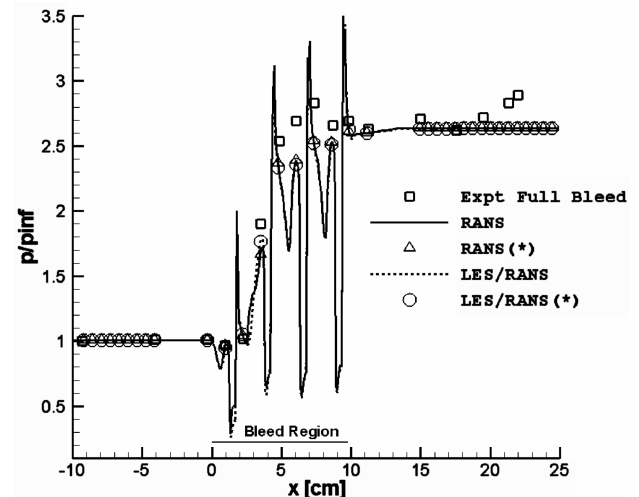


a) half bleed
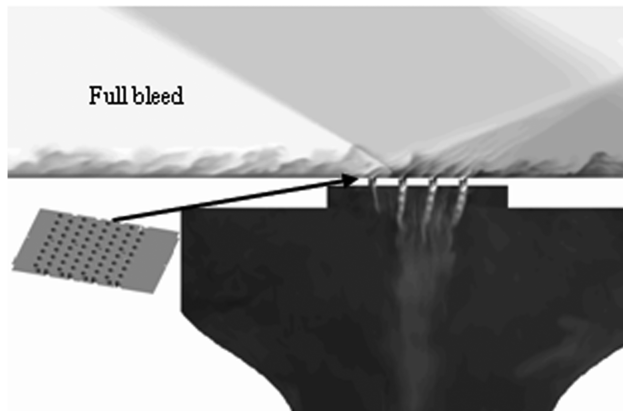


b) Full bleed

**Fig. 9  Snapshot of temperature contours with inset bleed plate: shock/boundary-layer interaction with bleed.**
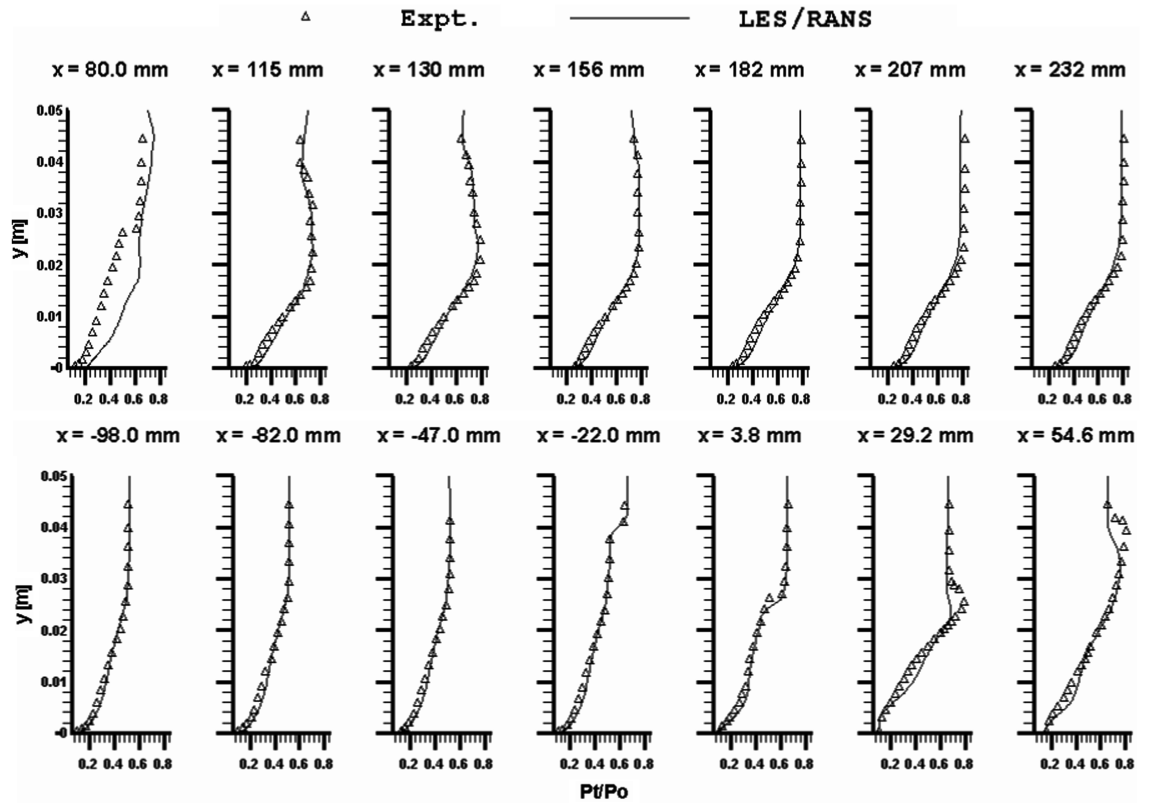


a) Half bleed



b) Full bleed

**Fig. 10  Wall pressure distributions: shock/boundary-layer interaction with bleed; (*): averaged at pressure tap locations.**

for the half-bleed case compared to the maximum-bleed scenario. This is due to the absence of active suction through the bleed ports in this region for the lower bleed rate. In [17], some discussion is made of the fact that the measured wall pressure for the maximum-bleed simulation is higher in some places than the value obtained through oblique-shock theory. The authors argue that situations might arise where, because of the suction effect, flow is directed into the static tap, causing it to read a higher value. Another explanation, furthered



a) Half bleed
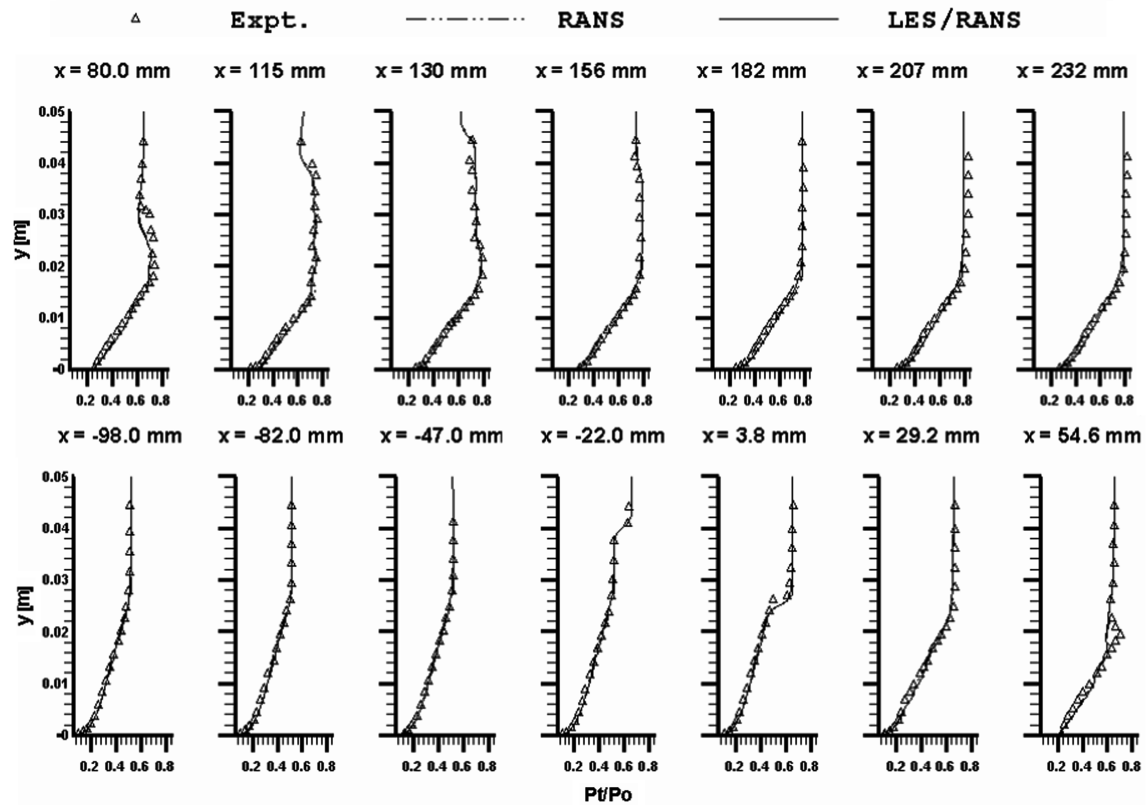


b) Full bleed

Fig. 11   Pitot pressure distributions: shock/boundary-layer interaction with bleed.

by the computational results, might be that some of the static taps are very close to a bleed hole and, as such, the static taps measure an average value associated with the rapid compression and expansion process occurring at the downstream edge of each bleed hole. It is clear that the bleed effects are highly localized, at least for this particular array.

Pitot pressure distributions throughout the interaction region are shown Fig. 11 for the LES/RANS and RANS simulations. The model predictions are very similar and agree well with the experimental data. The LES/RANS model produces a slightly fuller pitot pressure profile near the wall downstream of the bleed region for both the bleed rates. This result is consistent with that evidenced for the case without bleed, in that the LES/RANS model generally provides a more rapid recovery of the boundary layer downstream of a shock-induced disturbance. Predictions within in the interaction region, specifically at the 80 mm station, are not quite as good, especially for the half-bleed case. This is possibly due to the difference in the structure of the separation shock between experiment and that predicted by computation.

Pitot pressure distributions extracted at the bleed-hole exit plane (see Fig. 12) for the full-bleed case indicate that the computations underpredict the measured peak pressure level at all axial stations, with the LES/RANS model providing slightly better agreement. This trend is consistent with the underprediction of the overall bleed mass flow rate mentioned above. It is possible that these results would improve with additional X-Z mesh refinement over the holes.

Further details of the flow within the bleed holes are shown in Figs. 13 and 14. The bleed-mass-flux distributions over the entire array for the full- and half-bleed LES/RANS simulations are displayed in Fig. 13. Of particular note is the increase in bleed-mass flux in the region downstream of the shock-impingement location. This is the expected trend, as the pressure level is higher in this region. For the full-bleed case, the suction effect is much less for bleed ports located upstream of the shock-impingement location. The mass fluxes in this region are similar to those found in the flat-plate boundary-layer simulations discussed above. Some localized entrainment of bleed-hole fluid into the boundary layer is noted for the full-bleed case, but a much stronger blowing effect is present for the half-bleed case. This is due to a pressure differential within the plenum caused by the preferential injection of mass downstream of the shock-impingement location. Mach number contours and streamlines in Fig. 14 indicate that the initial entrainment of fluid into the bleed port occurs through a supersonic expansion that is terminated by a barrier shock [8] oriented normal to the flow direction. The lowermost portion of this shock wave interacts with the fluid near the upstream edge of the bleed port, creating a region of separation that acts to reduce the cross-sectional area occupied by the core fluid.
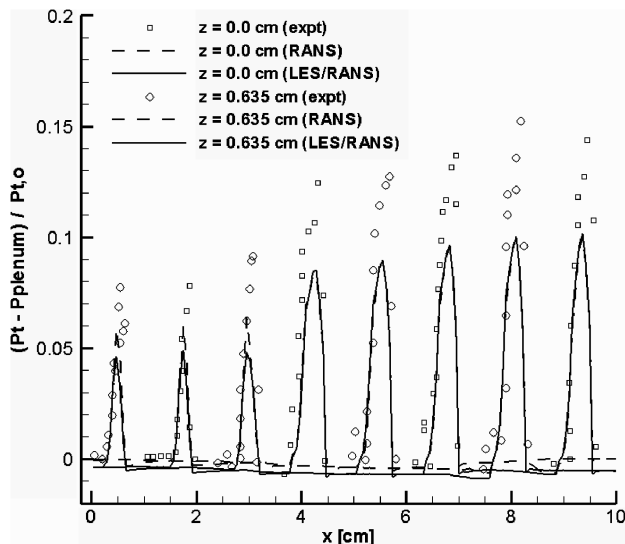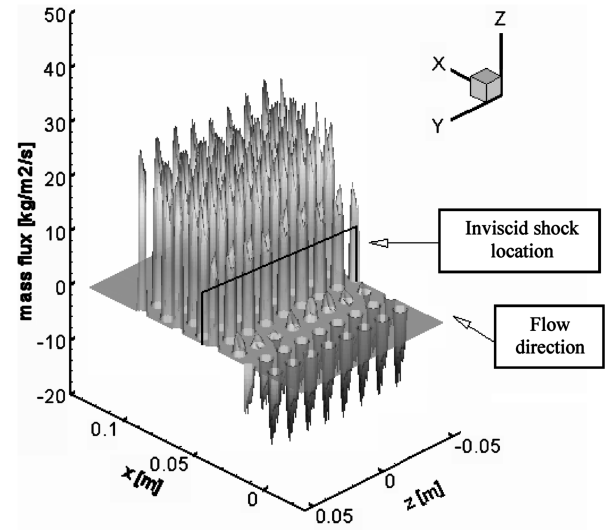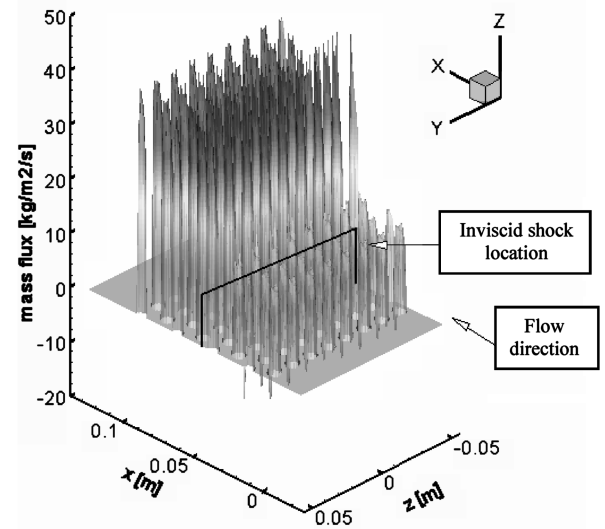


a) Half bleed



b) Full bleed

Fig. 13    Bleed-mass-flux distribution.



Fig. 12    Pitot pressure profiles at exit of bleed holes with full bleed.


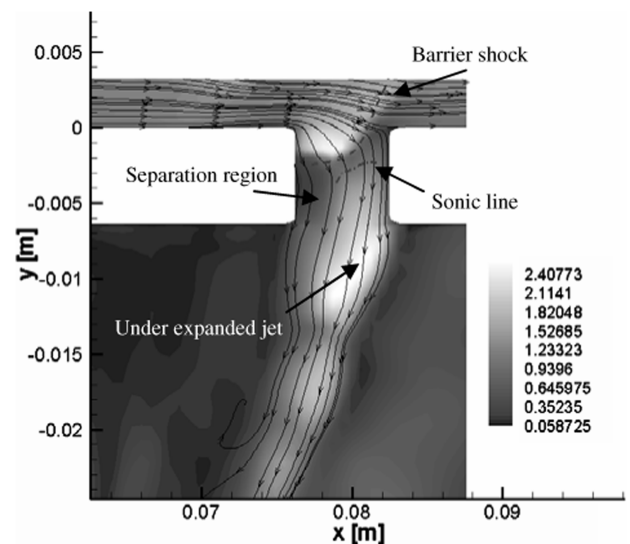
Fig. 14    Mach number contours in bleed hole.
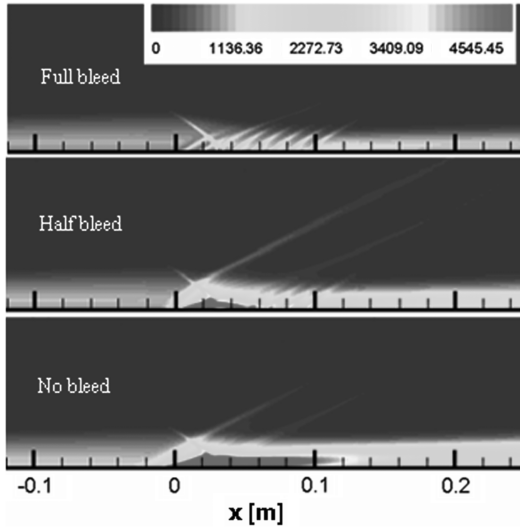
Fig. 15 Evolution of resolved turbulent kinetic energy through the interaction region.



Fig. 17 Isosurfaces of swirl strength $(10,000~\text{s}^{-1})$ for interactions with full bleed and no bleed.

The growth of this region creates an area minimum, which allows the subsonic flow behind the barrier shock to accelerate to supersonic speeds at the bleed-hole exit. This underexpanded jet then relaxes to the plenum pressure level through a series of expansion/compression waves. The uppermost portion of the barrier shock propagates out of the bleed port. The fluid that passes through this part of the barrier shock is compressed to levels in excess of the average wall pressure and is then expanded as it turns toward the flat-plate surface. This provides the mechanism for the large spikes in the wall pressure distributions shown in Fig. 10.

### D.   Reynolds-Stress Evolution and Turbulence Structure

Turbulence amplification is a well-known characteristic of shock/boundary-layer interactions. Bulk compression, streamline curvature, shock oscillation, and the dynamics of separation/reattachment all contribute to the amplification effect [28]. Large bleed rates as used in the Willis et al. [18] experiments can essentially remove turbulent separation but also induce other disturbances that could potentially amplify turbulence. Figures 15 and 16 plot span-averaged contours of resolved turbulence kinetic energy and resolved
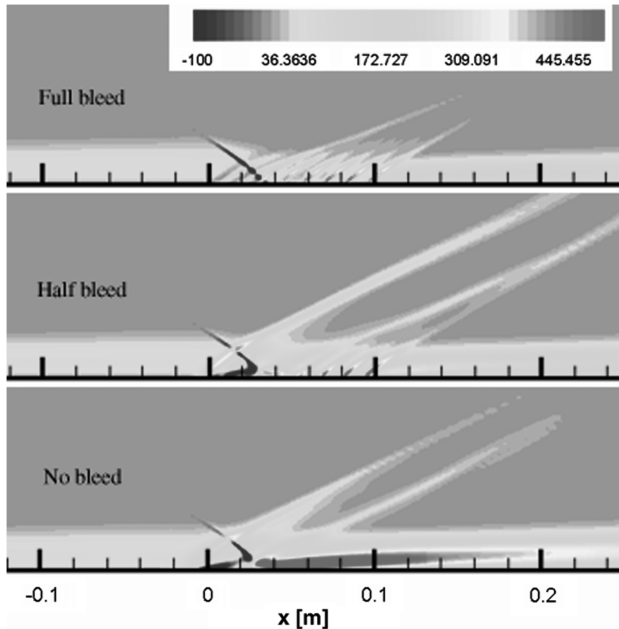
Reynolds shear stress $(\overline{\rho u'v'})$ for the LES/RANS cases with and without bleed. For the case without bleed, large Reynolds-stress values are found near the time-averaged position of the separation shock and downstream of the reattachment location. Further downstream, the stresses begin to relax to levels similar to, but larger than, those in the incoming boundary layer. With full bleed, the separation/reattachment response is eliminated, and very little Reynolds-stress



Fig. 16 Evolution of Reynolds shear-stress $\overline{\rho u'v'}$ through the interaction region.
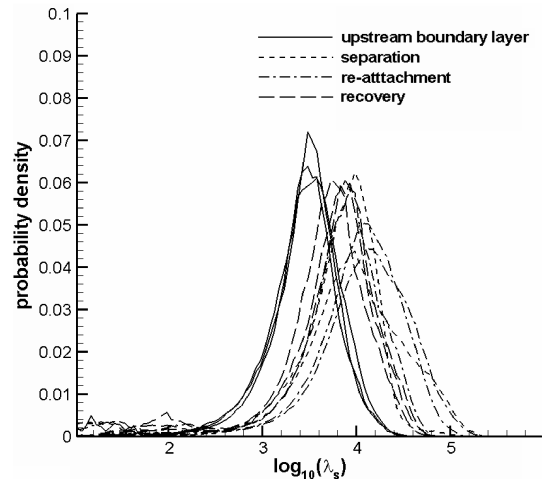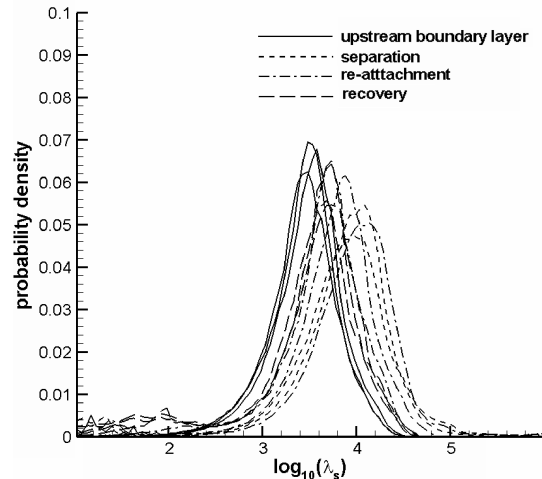


a) No bleed



Fig. 18 Evolution of swirl-strength probability density distributions.

amplification is observed. The half-bleed results indicate that some initial amplification takes place near and upstream of the shock-impingement position, as there is no significant suction effect in this region. Further downstream, the suction effect suppresses the shock system dynamics, and the Reynolds stresses again begin to relax to values similar to those in the upstream boundary layer. The wave patterns generated by flow into the bleed holes generate local disturbances in the Reynolds stresses, but these propagate out of the boundary layer. This result indicates that the dominant source of Reynolds-stress amplification in impinging-shock/boundary-layer interactions may be the dynamics of the separation region, which triggers the motion of the separation and reattachment shocks.

Figure 17 shows isosurfaces of the swirl strength ($10,000$ s$^{-1}$) for the interactions with and without full bleed. Visually, the interactions are similar, displaying a general increase in structural content and the presence of more smaller-scale structures within and downstream of the interaction region. A more quantitative measure, as shown in Fig. 18, is obtained by calculating the probability density function of the logarithm of the swirl strength at different streamwise locations. The most probable value is indicated as the peak in the distribution, and a shift in the distribution to the right implies an increase in the population of more tightly wrapped (finer-scale) vortical structures. This can also imply a general decrease in turbulence length scales. For the interaction without bleed, the most probable swirl-strength value increases by about an order of magnitude as the flow separates, then reattaches. In the recovery region, the most probable swirl-strength value decreases, and the distribution approaches that of the upstream boundary layer. With bleed, the distributions do not deviate as much in the interaction region, though the trend of an increasing population of finer-scale structures still holds. The swirl-strength distributions in the recovery region are close to those in the incoming boundary layer, again showing that the bleed effect accelerates the recovery of the boundary layer to a new equilibrium state following the shock reflection.

## V.  Conclusions

In this work, impinging-oblique-shock/turbulent-boundary-layer interactions with and without bleed have been simulated using the combination of immersed-boundary methods with LES/RANS and RANS turbulence models. Results have been compared to experimental data obtained at NASA GRC by Willis et al. [17,18]. The following observations may be stated:

1) The mass-conservative immersed-boundary method used in this work is an effective technique for simulating the effects of a large number of discrete bleed holes. Experimental discharge coefficients are slightly underpredicted but would probably improve with the use of a finer $X$-$Z$ mesh over each bleed port.

2) Both the Menter SST RANS model and the LES/RANS model provide excellent predictions of pitot pressure distributions throughout the interaction region, with and without boundary-layer bleed. Surface pressure distributions are better predicted by the Menter SST RANS model for the case without bleed.

3) At high-bleed rates, near-wall boundary-layer fluid expands supersonically into the bleed ports. A barrier shock compresses the fluid, and its interaction with the bleed-wall boundary layer forms a vena contracta that accelerates the core fluid to supersonic speeds as it exits the bleed port. The fluid that passes through the upper part of the barrier shock is compressed to levels in excess of the average wall pressure and is then expanded as it turns toward the flat-plate surface. This leads to pressure spikes that are partially captured in the experimental distributions.

4) Reynolds-stress predictions obtained from the LES/RANS model indicate that the use of boundary-layer bleed suppresses the amplification of turbulence often noted in shock/boundary-layer interactions. This result indicates that the dominant source of turbulence amplification in uncontrolled interactions may be the dynamics of the separation/reattachment event.

5) Swirl-strength probability density distributions indicate that the shock/boundary-layer interaction itself causes the formation of finer-scale vortical structures. The use of boundary-layer bleed accelerates

the recovery of the probability density distributions toward an equilibrium state similar to that in the incoming boundary layer.

6) The disturbances initiated by the Willis et al. [17,18] bleed-hole array are highly localized and are not representative of a continuous suction effect. This implies that existing models for boundary-layer bleed [29,30] may need to consider spatial variations in surface porosity, at least for arrays with larger bleed holes.

## References

[1]  Fukuda, M. K., Hingst, W. G., and Reshotko, E., "Control of Shock Wave–Boundary Layer Interactions by Bleed in Supersonic Mixed Compression Inlets," NASA CR-2595, Aug. 1975.

[2]  Syberg, J., and Konsek, J. L., "Bleed System Design Technology for Supersonic Inlets," *Journal of Aircraft*, Vol. 10, No. 7, 1973, pp. 407–413.
doi:10.2514/3.60241

[3]  Delery, J. M., "Shock Wave/Turbulent Boundary Layer Interaction and Its Control," *Progress in Aerospace Sciences*, Vol. 22, No. 4, 1985, pp. 209–280.
doi:10.1016/0376-0421(85)90001-6

[4]  Hamed, A., and Shang, J. S., "Survey of Validation Data Base for Shockwave Boundary-Layer Interactions in Supersonic Inlets," *Journal of Propulsion and Power*, Vol. 7, No. 4, 1991, pp. 617–625.
doi:10.2514/3.23370

[5]  Edwards, J. R., and McRae, D. S., "An Efficient Solution Technique for Shockwave–Boundary Layer Interactions with Flow Separation and Slot Suction Effects," AIAA Paper 91-0652, Jan. 1991.

[6]  Hamed, A., Shih, S., and Yeuan, J. J., "Investigation of Shock/Turbulent Boundary Layer Bleed Interactions," *Journal of Propulsion and Power*, Vol. 10, No. 1, 1994, pp. 79–87.
doi:10.2514/3.23714

[7]  Hamed, A., Yeuan, J. J., and Jun, Y. D., "Flow Characteristics in Boundary Layer Bleed Slots with Plenum," *Journal of Propulsion and Power*, Vol. 12, No. 2, 1996, pp. 231–236.
doi:10.2514/3.24018

[8]  Shih, T. I. P., Rimlinger, M. J., and Chyu, W. J., "3-Dimensional Shock-Wave Boundary Layer Interactions with Bleed," *AIAA Journal*, Vol. 31, No. 5, 1993, pp. 869–876.
doi:10.2514/3.11698

[9]  Rimlinger, M. J., Shih, T. I. P., and Chyu, W. J., "Shock-Wave Boundary Layer Interactions with Bleed Through Rows of Holes," *Journal of Propulsion and Power*, Vol. 12, No. 2, 1996, pp. 217–224.
doi:10.2514/3.24016

[10]  Hamed, A., and Zhisong, L., "Simulation of Bleed Hole Rows for Supersonic Turbulent Boundary Layer Control," AIAA Paper 2008-67, Jan. 2008.

[11]  Hingst, W. R., and Tanji, F. T., "Experimental Investigation of Two-Dimensional Shock–Boundary Layer Interaction with Bleed," AIAA Paper 83-0135, 1983; also NASA TM-83057, 1983.

[12]  Choi, J.-I., Oberoi, R. C., Edwards, J. R., and Rosati, J. A., "An Immersed Boundary Method for Complex Incompressible Flows," *Journal of Computational Physics*, Vol. 224, No. 2, 2007, pp. 757–784.
doi:10.1016/j.jcp.2006.10.032

[13]  Ghosh, S., and Edwards, J. R., "RANS and Hybrid LES/RANS Simulation of the Effects of Micro Vortex Generators Using Immersed Boundary Methods," AIAA Paper 2008-3738, June 2008.

[14]  Choudhari, M., Li, F., and Edwards, J. R., "Advanced Stability Analysis Pertaining to Laminar–Turbulent Transition in Hypersonic Boundary Layers," AIAA Paper 2009-0170, Jan. 2009.

[15]  Menter, F. R., "Two Equation Eddy Viscosity Turbulence Models for Engineering Applications," *AIAA Journal*, Vol. 32, No. 8, 1994, pp. 1598–1605.
doi:10.2514/3.12149

[16]  Edwards. J. R., Choi, J.-I., and Boles, J. A., "Hybrid LES/RANS Simulation of a Mach 5 Compression-Corner Interaction," *AIAA*

*Journal*, Vol. 46, No. 4, 2008, pp. 977–991.
doi:10.2514/1.32240

[17]  Willis, B. P., Davis, D. O., and Hingst, W. R., "Flow Coefficient Behavior for Boundary Layer Bleed Holes and Slots," NASA TM 106846, 1995; also AIAA Paper 1995-0031, 1995.

[18]  Willis, B. P., Davis, D. O., and Hingst, W. R., "Flowfield Measurements in a Normal-Hole-Bled Oblique Shock-Wave and Turbulent Boundary Layer Interaction," AIAA Paper 95-2885, 1995.

[19]  Edwards, J. R., "A Low-Diffusion Flux-Splitting Scheme for Navier–Stokes Calculations," *Computers and Fluids*, Vol. 26, No. 6, 1997, pp. 635–659.
doi:10.1016/S0045-7930(97)00014-5

[20]  Colella, P., and Woodward, P. R., "The Piecewise Parabolic Method (PPM) for Gas-Dynamical Simulations," *Journal of Computational Physics*, Vol. 54, No. 1, 1984, pp. 174–201.
doi:10.1016/0021-9991(84)90143-8

[21]  Edwards, J. R., "Numerical Simulations of Shock/Boundary Layer Interactions Using Time-Dependant Modeling Techniques—A Survey of Recent Results," AIAA Paper 2008-0525, Jan. 2008.

[22]  Lenormand, E., Sagaut, P., Ta Phuoc, L., and Comte, P., "Subgrid-Scale Models for Large-Eddy Simulations of Compressible Wall-Bounded Flows," *AIAA Journal*, Vol. 38, No. 8, 2000, pp. 1340–1350.
doi:10.2514/2.1133

[23]  Choi, J.-I., Edwards, J. R., and Baurle, R. A., "Compressible Boundary Layer Predictions at High Reynolds Number Using Hybrid LES/RANS Methods," AIAA Paper 2008-4175, Jan. 2008.

[24]  Xiao, X., Edwards, J. R., Hassan, H. A., and Baurle, R. A., "Inflow Boundary Conditions for Hybrid Large-Eddy/Reynolds-Averaged Navier–Stokes Simulations," *AIAA Journal*, Vol. 41, No. 8, 2003, pp. 1481–1490.
doi:10.2514/2.2130

[25]  Boles, J. A., Choi, J.-I., Edwards, J. R., and Baurle, R. A., "Simulations of High-Speed Internal Flows Using LES/RANS Models," AIAA Paper 2009-1324, Jan. 2009.

[26]  Walz, A., *Boundary Layers of Flow and Temperature*, MIT Press, Cambridge, MA, 1969.

[27]  Bond, R. B., and Edwards, J. R., "Computational Analysis of an Independent Ramjet Stream in a Combined Cycle Engine," *AIAA Journal*, Vol. 42, No. 11, 2004, pp. 2276–2284.
doi:10.2514/1.4465

[28]  Smits, A. J., and Muck, K.-C., "Experimental Study of Three Shock Wave/Turbulent Boundary Layer Interactions," *Journal of Fluid Mechanics*, Vol. 182, 1987, pp. 291–314.
doi:10.1017/S0022112087002349

[29]  Mayer, D. W., and Paynter, G. G., "Boundary Conditions for Unsteady Supersonic Inlet Analyses," *AIAA Journal*, Vol. 32, No. 6, 1994, pp. 1200–1206.
doi:10.2514/3.12120

[30]  Slater, J. W., and Saunders, J. D., "Modeling of Fixed-Exit Porous Bleed Systems," AIAA Paper 2008-0094, Jan. 2008.

J. Oefelein
*Associate Editor*